Generalised Acoustic Analogy Modelling of Hot Jet Noise

V. Gryazev,[1]

School of Engineering and Material Science, Queen Mary University of London, London, E1 4NS, UK,

A.P. Markesteijn[2,4], and S.A Karabasov[3,4]

School of Engineering and Material Science, Queen Mary University of London, London, E1 4NS, UK,

GPU-prime Ltd, Cambridge, UK

A generalised acoustic analogy model is implemented for the hot and cold static high-speed jet cases corresponding to conditions of the SILOET experiment performed by QinetiQ. The model is statistical and based on the covariance of fluctuating Reynolds stresses and enthalpy source terms in accordance with Goldstein's theory. These quantities are obtained from a solution of the validated Large Eddy Simulation (LES) accelerated on Graphics Processing Units (GPU). The covariance of fluctuating enthalpy terms is represented by the Khavaran and Bridges model, which involves the velocity autocorrelation function and temperature gradient in the jet. The velocity autocorrelation function and the covariance of fluctuating Reynolds stresses are approximated by an analytical Gaussian-exponential function. The input parameters of the acoustic model include single-point quantities such as the time-averaged local stream-wise velocity, sound speed, temperature, vorticity magnitude, turbulent kinetic energy, and dissipation rate. Modelling choices for the acoustic length and time scales based on either the turbulent kinetic energy

[1] Post-Doctoral Researcher, School of Engineering and Material Sciences, Mile End Road, London, E1 4NS, UK.
[2] Post-Doctoral Researcher, School of Engineering and Material Sciences, Mile End Road, London, E1 4NS, UK
[3] Professor, School of Engineering and Material Sciences, Mile End Road, London, E1 4NS and AIAA Associate Fellow
[4] Research Scientist / Director, GPU-prime Ltd.

dissipation rate or meanflow vorticity are discussed. In each case, the model involves two dimensionless parameters associated with the acoustic correlation length and time scale. These two parameters are calibrated based on the far-field noise data at 90º observer angle. The sensitivity of the calibration coefficients to the jet type, cold vs. hot is investigated. Furthermore, the same acoustic model without re-calibration is applied for far-field noise predictions of two NASA (Small Hot Jet Acoustic Rig) SHJAR jets for acoustic Mach numbers 0.5 and 0.9. To probe the sensitivity of the acoustic model to the input flow data, Reynolds Averaged Navier-Stokes (RANS) solutions of the same jet cases are considered along with the LES solutions. The comparison of the predicted far-field noise spectra with the experiment is discussed in each case.

I.Introduction

The effect of jet temperature on mixing noise in hot jets has been recognised since 1970s [1] and continues to be a subject of the active research today [2-6]. Jet heating affects both the modification of jet turbulence in the flow and the change in sound mean-flow propagation due to both the non-uniform mean-flow velocity distribution and the local sound speed in the "thermal layers".

In many hot jet noise prediction schemes, hybrid solution methods are used wherein the computation process is decoupled into a non-linear flow model in the jet region and a linear sound propagation model. The decomposition into the non-linear and linear solution regions can be done in a variety of ways.

In the framework of the phenomenological approach, Tam and co-workers [7, 8] distinguished two independent jet noise mechanisms and modelled them statistically. One mechanism is associated with the fine-scale turbulence by analogy with the kinetic gas theory and the other is directly linked to linear instability waves, e.g. noise radiated by large-scale coherent structures. More recently, the importance of the second mechanism has been re-argued in the framework of a dynamic model based on the wavepacket

theory, which identifies coherent structures in the jet, and which can be directly related to the far-field sound via a Green's function or Kirchhoff's method [9].

In comparison with the phenomenological approach, the method of acoustic analogy is based on a systematic rearrangement of the governing Navier-Stokes equations to linear sound propagation equation and the right-hand-side terms. The latter terms are grouped together as an effective source, which does not depend on the linear propagation. Following this approach, the linear propagation problem is solved with an appropriate Green's function method, which leads to the far-field acoustic integral. The acoustic integral involves covariances of the turbulent stresses and other terms, which are modelled statistically. Acoustic analogy methods were pioneered by Lighthill [10], who had considered the linear wave equation as the sound propagation model, which simplicity makes it amenable to analytical solution. In more recent formulations of the acoustic analogy method, meanflow effects were included in the linear propagation model thereby simplifying the modelling of the source terms. Most notably, Lilley [11] pointed out at the importance of meanflow refraction effect for jet noise propagation in the small angles to the jet flow. Ffowcs Williams [12] made another seminal contribution to the acoustic analogy method by considering the effect of moving sound sources, which led to the development of the Ffowcs Williams – Hawkings (FW-H) method [13] — a very popular integral surface method for numerical calculation of noise generated by aerodynamic flows. In comparison with the earlier acoustic analogy formulations, the Generalised Acoustic Analogy (GAA) developed by Goldstein [14, 15, 16] can be considered as the most complete acoustic analogy model up to date. It incorporates the linearised Euler equations as the linear propagation operator, which shares the same linear hyperbolic part with the governing Navier-Stokes equations. This formulation greatly simplifies modelling of the effective nonlinear source terms, which correspond to the right-hand-side of the GAA equations. These GAA terms correspond to the fluctuating Reynolds stresses and the fluctuating enthalpy term, which are directly related to the jet turbulence rather than to the acoustic solution component. By using a scalar product of the source terms of different directivity with components of the vector adjoint Green's function, the GAA approach allows to capture the complete directivity of jet noise from small to large polar angles relative to the downstream the jet axis [16, 17].

In the previous works, the source terms of the GAA models were modelled statistically either via a hybrid approach where the Large Eddy Solution (LES) was used to inform the Reynolds Averaged Navier-Stokes (RANS) model [18, 19] or reconstructed directly from LES [20, 21]. In each case, LES played a major role by providing the key information about the amplitudes (and length scales, if available) of various terms corresponding to different acoustic directivity. Up to date, all LES-based implementations of the GAA models were focused on cold jet noise modelling. Hence, one goal of the current work is to extend this class of GAA models to hot jet noise. For validation, the hot and cold high-speed jet cases of the Roll-Royce SILOET (Strategic Investment in Low-carbon Engine Technology) jet experiment performed by QinetiQ [22] are considered. In the SILOET experiment, single-stream jets issue from a profiled convergent nozzle at the same acoustic Mach number of 0.875. The flow field solutions are obtained using LES and RANS solutions, which are cross-validated and used in the acoustic modelling.

For the sake of simplicity, inevitably, the GAA model implementation requires a few calibrations based on the introduction of effective non-dimensional space and time acoustic length scale parameters. Hence, to address the question how general the derived acoustic length scale parameters are, the sensitivity of the calibration parameters is first analysed between the hot and the cold jet cases of the SILOET experiment. The generality of the developed acoustic model is put up for a further test by applying the same model parameters to predict far-field noise spectra of the two NASA (Small Hot Jet Acoustic Rig) SHJAR jets corresponding to acoustic Mach numbers 0.5 and 0.9 [23, 24].

The current article presents an extended analysis using both the RANS and the LES solutions and considers alternative choices for modelling of the acoustic correlation scales. A preliminary version of this work was reported in [25].

II.Goldstein Generalized Acoustic Analogy

Following [14] and [18], which provide a simpler form of the generalised acoustic analogy equations in comparison with a more general but less explicit formulation [16], time-averaged, Favre-averaged mean-flow, and fluctuation variables are introduced

$$\rho' = \rho - \overline{\rho}, \quad p' = p - \overline{p}, \quad v_i' = v_i - \tilde{v}_i, \quad h' = h - \tilde{h}, \tag{1}$$

where ρ, p, v_i and h refers to density, pressure, Cartesian velocity component $(i = 1,2,3)$, and enthalpy, respectively. Primes denote fluctuations, and bar and tilde correspond to time and Favre averaging.

By defining the momentum perturbation variable

$$u_i = \rho v_i', \tag{2}$$

the governing Euler equations in position $(\mathbf{y}, \tau)$ are re-arranged to

$$\begin{gathered}
\frac{\partial \rho'}{\partial \tau} + \frac{\partial}{\partial y_j}(\rho' \tilde{v}_j + u_j) = 0, \\
\frac{\partial u_i}{\partial \tau} + \frac{\partial}{\partial y_j}(\tilde{v}_j u_i) + \frac{\partial p'}{\partial y_i} + u_j \frac{\partial \tilde{v}_i}{\partial y_j} - \frac{\rho'}{\overline{\rho}} \frac{\partial \tilde{\tau}_{ij}}{\partial y_j} = \frac{\partial T_{ij}'}{\partial y_j}, \\
\frac{1}{\gamma - 1}\left(\frac{\partial p'}{\partial \tau} + \frac{\partial}{\partial y_j}(p' \tilde{v}_j) \right) + \frac{\partial}{\partial y_j}(u_j \tilde{h}) + p' \frac{\partial \tilde{v}_j}{\partial y_j} - \frac{u_i}{\overline{\rho}} \frac{\partial \tilde{\tau}_{ij}}{\partial y_j} = Q,
\end{gathered} \tag{3}$$

where

$$\begin{gathered}
\tilde{h}_0 = \tilde{h} + \frac{1}{2} |\, \tilde{\mathbf{v}} \,|^2, \quad h_0' = h' + \tilde{v}_i v_i' + \frac{1}{2} |\, \mathbf{v}' \,|^2, \\
T_{ij}' = -\left(\rho v_i' v_j' - \widetilde{\overline{\rho} v_i' v_j'} \right), \quad H_i' = -\left(\rho v_i' h_0' - \widetilde{\overline{\rho} v_i' h_0'} \right), \\
Q = -\tilde{v}_j \frac{\partial T_{ij}'}{\partial y_i} + \frac{1}{2} \delta_{ij} \left[\frac{\partial}{\partial \tau} T_{ij}' + \tilde{v}_k \frac{\partial}{\partial y_k} T_{ij}' + \frac{\partial \tilde{v}_k}{\partial y_k} T_{ij}' \right] + \frac{\partial}{\partial y_i} H_i', \\
i, j, k, l = 1,2,3.
\end{gathered} \tag{4}$$

In the last equation (3), $\tilde{\tau}_{ij} = \delta_{ij} \overline{p}$ corresponds to the inviscid part of the Reynolds stress. Following the Einstein notation here and in other parts of the paper, summation over a repeated index is assumed.

Once the source terms of the linearised Euler equations (2)-(4) are obtained from a separate model independently of the left-hand-side part, the sources can be substituted in (4) to solve the equations in the entire solution domain including the acoustic pressure solution component for a far-field observer location. To facilitate the modelling, the solution of the propagation problem can be completely decoupled from the right-hand-side using the tensor Green's function method. In the latter method, the governing linear equations (2) and (3) are solved with point sources in the momentum and energy equations. As explained in [26] for the linearised Euler system, this amounts to solving the governing partial differential equations 4 times corresponding to 3 momentum equations and 1 energy equation per each source location. Furthermore, jet noise is typically characterized by distributed sources, hence, this approach implies a significant number of source locations, which need to be considered. Altogether, this makes the solution process based on the tensor Green's function approach very inefficient. On the other hand, if only a few locations where the far-field pressure needs to be computed are of interest, a very elegant vector adjoint Green's function technique can be used to significantly reduce the amount of calculations. Using this technique, the corresponding adjoint equations are solved only once for each observer location. The technique is based on the general reciprocity principle in mechanics using Lagrange's identity between the solutions of the direct and the adjoint problem with introducing a suitable scalar product of the corresponding operators [27],

$$\left\langle \begin{pmatrix} \rho^{(a)} \\ \mathbf{v}^{(a)} \\ p^{(a)} \end{pmatrix}, \mathbf{L} \begin{pmatrix} \rho \\ \mathbf{u} \\ p \end{pmatrix} \right\rangle = \left\langle \mathbf{L}^{(a)} \begin{pmatrix} \rho^{(a)} \\ \mathbf{v}^{(a)} \\ p^{(a)} \end{pmatrix}, \begin{pmatrix} \rho \\ \mathbf{u} \\ p \end{pmatrix} \right\rangle \tag{5}$$

where $\mathbf{L}$ stands for the linearised Euler operator, which acts on the density ρ momentum vector $\mathbf{u}$, and pressure p fluctuation variables of the left-hand-side of (3), $p^{(a)}$, $\mathbf{v}^{(a)}$ and $\rho^{(a)}$ are the corresponding adjoint variables, and brackets $\langle , \rangle$ correspond to integration over the source and observer space and time coordinates. Here, suitable boundary conditions are assumed so that the corresponding surface integrals, which emerge when re-arranging the left-hand-side of (5) to its right-hand-side by integration by parts, disappear.

From the above Lagrange's identity, the corresponding adjoint linearised Euler operator, $\mathbf{L}^{(a)}$ is defined. As noted in [26], $\mathbf{L}$ corresponds to the direct problem of noise radiation by the jet, $\mathbf{L}^{(a)}$ corresponds to the adjoint problem of sound scattering, where a point sink is put in the far-field observer location, $\mathbf{x}$, and the time flow in the adjoint problem reverses in comparison with the direct problem. In the frequency domain, the equations for the vector adjoint linearised Euler Green's function $\left(\hat{\rho}^{(a)}, \hat{v}_j^{(a)}, \hat{p}^{(a)}\right)(\mathbf{y}, \omega \,|\, \mathbf{x})$ for the Goldstein generalised acoustic analogy are given by [18].

$$
\begin{aligned}
&\mathrm{i}\omega\hat{\rho}^{a} + \tilde{v}_j \frac{\partial}{\partial y_j}\hat{\rho}^{(a)} + \frac{\hat{v}_i^{(a)}}{\bar{\rho}}\frac{\partial \tilde{\tau}_{ij}}{\partial y_j} = 0,\\
&\mathrm{i}\omega\hat{v}_j^{(a)} + \frac{\partial}{\partial y_j}\hat{\rho}^{(a)} + \tilde{v}_i \frac{\partial}{\partial y_j}\hat{v}_i^{(a)} - \hat{v}_i^{(a)}\frac{\partial \tilde{v}_i}{\partial y_j} + \tilde{h}\frac{\partial}{\partial y_j}\hat{p}^{(a)} + \frac{\hat{p}^{(a)}}{\bar{\rho}}\frac{\partial \tau_{ij}}{\partial y_i} = 0,\\
&\left(\frac{\mathrm{i}\omega}{\gamma - 1}\right)\hat{p}^{(a)} + \left(\frac{\tilde{v}_j}{\gamma - 1}\right)\frac{\partial}{\partial y_j}\hat{p}^{(a)} - \hat{p}^{(a)}\frac{\partial \tilde{v}_j}{\partial y_j} + \frac{\partial}{\partial y_j}\hat{v}_j^{(a)} = \delta(\mathbf{y} - \mathbf{x}).
\end{aligned}
\tag{6}
$$

In the above equations, $\hat{\rho}^{(a)}, \hat{v}_j^{(a)}, \hat{p}^{(a)}$ are the corresponding Fourier transforms of the adjoint density, velocity, and pressure solution components.

Under the locally parallel axisymmetric flow approximation, which will be used in this work, the adjoint linearised Euler equations in the cylindical-polar coordinates of the jet (Fig.1) reduce to

$$
\begin{aligned}
&\mathrm{i}\omega\hat{v}_1^{(a)} + \tilde{v}_1\frac{\partial}{\partial y_1}\hat{v}_1^{(a)} + \left(\frac{\widetilde{c^2}}{\gamma - 1}\right)\frac{\partial}{\partial y_1}\hat{p}^{(a)} = 0,\\
&\mathrm{i}\omega\hat{v}_r^{(a)} + \tilde{v}_1\frac{\partial}{\partial y_1}\hat{v}_r^{(a)} - \hat{v}_1^{(a)}\frac{\partial \tilde{v}_1}{\partial y_r} + \left(\frac{\widetilde{c^2}}{\gamma - 1}\right)\frac{\partial}{\partial r}\hat{p}^{(a)} = 0,\\
&\mathrm{i}\omega\hat{v}_\theta^{(a)} + \tilde{v}_1\frac{\partial}{\partial y_1}\hat{v}_\theta^{(a)} + \left(\frac{\widetilde{c^2}}{\gamma - 1}\right)\frac{\partial}{r\partial\theta}\hat{p}^{(a)} = 0,\\
&\left(\frac{\mathrm{i}\omega}{\gamma - 1}\right)\hat{p}^{(a)} + \left(\frac{\tilde{v}_1}{\gamma - 1}\right)\frac{\partial}{\partial y_1}\hat{p}^{(a)} + \frac{\partial}{\partial y_1}\hat{v}_1^{(a)} + \frac{\partial}{r\partial r}\left(r\hat{v}_r^{(a)}\right) + \frac{\partial}{r\partial\theta}\hat{v}_\theta^{(a)} = \delta(\mathbf{x} - \mathbf{y}),
\end{aligned}
\tag{7}
$$

where $\hat{v}_1^{(a)}, \hat{v}_r^{(a)}, \text{and } \hat{v}_\theta^{(a)}$ are the adjoint-velocity components in the cylindrical polar coordinate system (Fig. 1) and $\tilde{v}_1 = \tilde{v}_1\left(Y_1, r\right)$ and $\widetilde{c^2} = \widetilde{c^2}\left(Y_1, r\right)$ are local radial distributions of the axial velocity and square

of the sound speed for each slowly varying streamwise variable which is related to the unscaled one through the small ($O(\varepsilon)$) jet spread rate $Y_1 = \varepsilon y_1$.

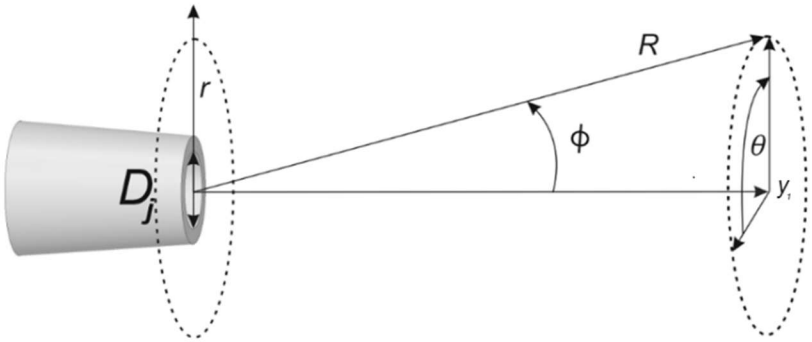

Fig. 1 Definition of the cylindrical-polar coordinate system for acoustic modelling.

Following [26], the above equations can be rearranged into ordinary differential equations (ODEs) for amplitudes of the azimuthal solution modes, where it is sufficient to use only the even part of the Fourier decomposition because of the axisymmetric meanflow of the jet

$$(\hat{\rho}_n^{(a)}, \hat{v}_{1,n}^{(a)}, \hat{v}_{r,n}^{(a)}, \hat{v}_{\theta,n}^{(a)}, \hat{p}_n^{(a)}) = \sum_{n=0}^{\infty} \left(\hat{\rho}_n^{(a)} \cos(n\theta), \hat{v}_{1,n}^{(a)} \cos(n\theta), \hat{v}_{r,n}^{(a)} \cos(n\theta), \hat{v}_{\theta,n}^{(a)} \sin(n\theta), \hat{p}_n^{(a)} \cos(n\theta) \right). \tag{8}$$

For solution, the jet flow is divided into a sufficient number of sections along the jet stream-wise coordinate $Y_1 = \varepsilon y_1$ in order to ensure that the stream-wise variation of the jet profile is well captured. Each of these non-overlapping sections corresponds to a piece-wise constant flow field where the velocity and the sound speed are functions of radius only. For each jet section, periodic boundary conditions are assumed in the stream-wise jet direction. The resulting second-order ODE is integrated numerically at high accuracy using the fourth-order Runge-Kutta method. The combined solution for the amplitude distribution of each azimuthal mode is composed from the individual sections and is a function of radius and axial location in the jet. The entire process for 20 frequencies and 10 azimuthal models takes several minutes in MATLAB. It can be also noted that the solution process is equivalent to numerically solving a series of Lilley's equations for a specified frequency response, one for each section of the jet.

The following expression in terms of the adjoint Green's function for the far-field pressure is obtained:

$$\hat{p}(\mathbf{x},\omega)=\int_V\left(\hat{v}_i^{(a)}(\mathbf{y},\omega\,|\,\mathbf{x})\frac{\partial T_{ij}}{\partial y_j}(\mathbf{y},\omega)+p^{(a)}(\mathbf{y},\omega\,|\,\mathbf{x})Q(\mathbf{y},\omega)\right)d\mathbf{y}, \tag{9}$$

where $\hat{T}_{ij}$ and Q are the Fourier transforms of the source terms. Applying the integration by parts to remove derivatives from the source terms and assuming that the covariance of the fluctuating Reynolds stresses in the momentum equation and the fluctuating enthalpy stresses is negligible in comparison with those of the terms of the same type [5, 25, 28], the far-field sound pressure spectral density breaks down into 'cold' and 'hot' source contributions,

$$S(\mathbf{x},\omega)=S^{(\mathrm{cold})}+S^{(\mathrm{hot})}, \tag{10}$$

where

$$S^{(\mathrm{cold})}=\int_V\int_V\hat{R}_{ijkl}(\mathbf{y},\boldsymbol{\Delta},\omega)\hat{I}_{ij}(\mathbf{y},\omega\,|\,\mathbf{x})\hat{I}^*_{kl}(\mathbf{y}+\boldsymbol{\Delta},\omega\,|\,\mathbf{x})d(\boldsymbol{\Delta})d\mathbf{y} \tag{11}$$

and

$$S^{(\mathrm{hot})}=\int_V\int_V\hat{H}_{ij}(\mathbf{y},\boldsymbol{\Delta},\omega)\hat{I}_{i}(\mathbf{y},\omega\,|\,\mathbf{x})\hat{I}^*_{j}(\mathbf{y}+\boldsymbol{\Delta},\omega\,|\,\mathbf{x})d(\boldsymbol{\Delta})d\mathbf{y}, \tag{12}$$

where the integral kernels include Fourier transforms of the corresponding covariance terms, and where V is a jet volume.

$$\hat{R}_{ijkl}(\mathbf{y},\boldsymbol{\Delta},\omega)=\int_{-\infty}^{\infty}R_{ijkl}(\mathbf{y},\boldsymbol{\Delta},\tau)e^{i\omega\tau}d\tau,\quad\text{and}\quad\hat{H}_{ij}(\mathbf{y},\boldsymbol{\Delta},\omega)=\int_{-\infty}^{\infty}H_{ij}(\mathbf{y},\boldsymbol{\Delta},\tau)e^{i\omega\tau}d\tau. \tag{13}$$

Here «∗» denotes complex conjugate and the covariance functions are

$$R_{ijkl}(\mathbf{y},\boldsymbol{\Delta},\tau)=\overline{T'_{ij}(\mathbf{y},t)T'_{kl}(\mathbf{y}+\boldsymbol{\Delta},t+\tau)},\ \text{and}\ H_{ij}(\mathbf{y},\boldsymbol{\Delta},\tau)=\overline{H'_{i}(\mathbf{y},t)H'_{j}(\mathbf{y}+\boldsymbol{\Delta},t+\tau)}, \tag{14}$$

overbars stand for time averaging, t, and indices $i,j,k,l=1,2,3$ correspond to 3D Cartesian space.

The propagator terms of the sound integral (11) and (12) are given by

$$\hat{I}_{ij}(\mathbf{y},\omega\,|\,\mathbf{x})=\frac{\partial\hat{v}_j^{(a)}(\mathbf{y},\omega\,|\,\mathbf{x})}{\partial y_i}-\left[\frac{\partial\tilde{v}_j}{\partial y_i}(\mathbf{y})\,p^{(a)}(\mathbf{y},\omega\,|\,\mathbf{x})+\tilde{v}_j\frac{\partial p^{(a)}(\mathbf{y},\omega\,|\,\mathbf{x})}{\partial y_i}\right]$$
$$+\frac{\delta_{ij}}{2}\left(i\omega+\tilde{v}_k\frac{\partial}{\partial y_k}\right)p^{(a)}(\mathbf{y},\omega\,|\,\mathbf{x}), \tag{15}$$

and

$$\hat{I}_i\,(\mathbf{y},\omega\,|\,\mathbf{x})=-\frac{\partial p^{(a)}(\mathbf{y},\omega\,|\,\mathbf{x})}{\partial y_i}\,. \tag{16}$$

By transforming to the cylindrical-polar coordinates, the propagator tensor in (11) is decomposed into cylindrical modes,

$$\hat{I}_{ij}=\sum_{n=0}^{\infty}\hat{I}_{ij,n}\,,\ i,j=1,2,3\,, \tag{17}$$

where the individual mode components are

$$\hat{\mathbf{I}}_n=\begin{pmatrix} a_{11,n}\cos(n\theta) & a_{12,n}\cos(n\theta) & a_{13,n}\sin(n\theta)\\ a_{21,n}\cos(n\theta) & a_{22,n}\cos(n\theta) & a_{23,n}\sin(n\theta)\\ a_{31,n}\sin(n\theta) & a_{32,n}\sin(n\theta) & a_{33,n}\cos(n\theta)\end{pmatrix} \tag{18}$$

Here n is the azimuthal mode number, and the azimuthal mode coefficients are expressed via components of the adjoint Green's function as follows:

$$\left(a_{ij,n}\right)=\begin{pmatrix} \left(\frac{\partial\hat{v}_{1,n}^a}{\partial y_1}+\gamma_n\right) & \frac{\partial\hat{v}_{r,n}^a}{\partial y_1} & \frac{\partial\hat{v}_{\theta,n}^a}{\partial y_1}\\ \left(\frac{\partial\hat{v}_{1,n}^a}{\partial r}-\frac{\partial\tilde{v}_1}{\partial r}\hat{p}_n^a-\tilde{v}_1\frac{\partial\hat{p}_n^a}{\partial r}\right) & \left(\frac{\partial\hat{v}_{r,n}^a}{\partial r}+\gamma_n\right) & \frac{\partial\hat{v}_{\theta,n}^a}{\partial r}\\ -\frac{n}{r}(\hat{v}_{1,n}^a-\tilde{v}\hat{p}_n^a) & \left(-\frac{n}{r}\hat{v}_{r,n}^a-\frac{1}{r}\hat{v}_{\theta,n}^a\right) & \left(\frac{n}{r}\hat{v}_{\theta,n}^a+\frac{1}{r}\hat{v}_{r,n}^a+\gamma_n\right)\end{pmatrix}, \tag{19}$$

$$\gamma_n=\frac{1}{2}\left(i\omega\hat{p}_n^a+\tilde{v}_1\frac{\partial\hat{p}_n^a}{\partial y_1}\right),$$

where the adjoint velocity components of the Green's function correspond to the selected polar coordinate system.

Following the same procedure for the propagator vector in (12), the decomposition into cylindrical modes yields

$$\hat{I}_i = \sum_{n=0}^{\infty} \hat{I}_{i,n}, \quad i = 1,2,3, \tag{20}$$

where the individual mode components are

$$\hat{\mathbf{I}}_n = \left(b_{1,n} \cos n\theta \quad b_{2,n} \cos n\theta \quad b_{3,n} \sin n\theta \right). \tag{21}$$

Here the mode coefficients are related to the adjoint Green's function components in accordance with

$$\left(b_{i,n} \right) = -\left(\frac{\partial \hat{p}_n^{(a)}}{\partial y_1} \quad \frac{\partial \hat{p}_n^{(a)}}{\partial r} \quad -\frac{n}{r} \hat{p}_n^{(a)} \right). \tag{22}$$

III. Jet Flow Modeling

The cold and hot jet flows correspond to conditions of the cold and hot SILOET jet cases [22], which operating conditions are summarised in Table 1.

Table 1. The operating conditions of SILOET jet.

	U_j	M_j	T_j / T_0	$\mathrm{Re} = U_j D_j / \nu$
Cold	297	0.875	1	$2 \cdot 10^6$
Hot	297	0.55	2.5	$5 \cdot 10^5$

For both the jet cases, Large Eddy Simulations are performed based on the Compact Accurately Boundary-Adjusting high-REsolution Technique (CABARET) method [29], [30], [31]. CABARET is a shock-capturing scheme with improved dissipation and dispersion properties and implemented with asynchronous time stepping [32]. All simulations correspond to the Monotonically Integrated LES (MILES) framework [33], which was previously applied for the same jet cases in [34]. Graphics Processing Units (GPU) are utilised to reduce the flow solution time to 2 days per case [35, 36]. Unstructured meshes

based on the OpenFOAM snappyHexMesh utility are used for generating patches of locally refined uniform Cartesian grid in the location of early shear layers. In comparison to a multi-block structured grid, snappyHexMesh allows to generate a more-or-less isotropic grid near the nozzle lip [37] of a high density, $dy_1 / D_j = dy_2 / D_j = dy_3 / D_j = 0.002$. The stream-wise extent of the computational domain is about $100D_j$ and the radial size is $30D_j$, which results in the total LES grid count of about $90 \cdot 10^6$ control volumes. No information about the boundary layer state upstream of the nozzle exit is available in the SILOET experiment, hence, an initially laminar jet inflow condition is imposed upstream of the nozzle exit for simplicity. For the lateral and downstream boundaries of the open domain, characteristic boundary conditions are used following [31] in order to minimise artificial reflections.

For far-field noise calculations, the standard penetrable-surface formulation of the FW-H method [13] is applied. Following the common practice in jet noise modelling, the acoustic integration surfaces are constructed to be of a funnel shape with sides parallel to the jet shear layers and should include all important jet noise sources (Fig.2). The funnel surface is terminated with 16 closing discs at the outlet. The surface is selected to exclude vortices crossing the acoustic surfaces apart from much further downstream of the potential core of the jet. In the downstream part of the FW-H surface, most of the pseudo-sound artefacts caused by the vortices crossing the outlet control surface are avoided by averaging the noise signals produced by each individual disc following [31, 38]. The LES grid resolution is maintained reasonably fine in the vicinity of the control surface location so that it supports acoustic wave propagation with 10 points per wavelength at $St_D = 10$ in the vicinity of the initial shear layers and at $St_D = 2$ in the vicinity of the end of the potential core length of the jet. The LES solutions are computed for 600 convective Time Units, TU ($1\ \mathrm{TU} = D_j / U_j$), which takes two days per jet case on a workstation equipped with two NVidia Titan RTX cards (24GB). 200 TUs correspond to the initial solution spinout time and 400 TUs are used for the statistical averaging.

In the absence of flow data from the experiment, for validation of the noise spectra predictions of the current LES solutions, the spectra predictions are compared with the available acoustic measurements of

the SILOET experiment and also the predictions of the NASA sJet model [39], [40]. The latter is an empirical scaling-law model based on interpolation and calibrated on a large database of NASA jet cases of various Mach numbers and temperature ratios.

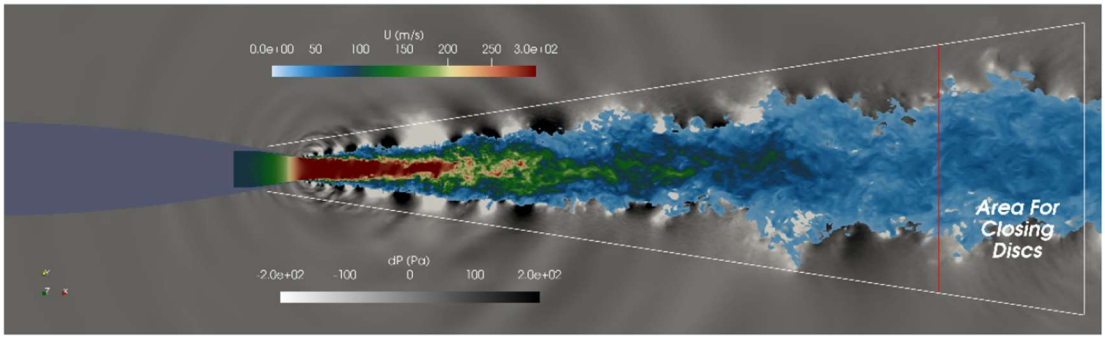

Fig. 2 The LES flow and acoustic pressure solution around the jet: instantaneous axial velocity component and pressure distributions with a superimposed contour of the acoustic integration surface of the FW-H method

The comparison of acoustic spectra predictions of cold and hot SILOET jets for three polar angles, 30º, 60º and 90º with experiment and sJet code are shown in Figures 3 and 4. For computing the spectra from the time signal, the standard Welch method of Fourier transforms of short periodograms is used, which implementation details can be found in [37].

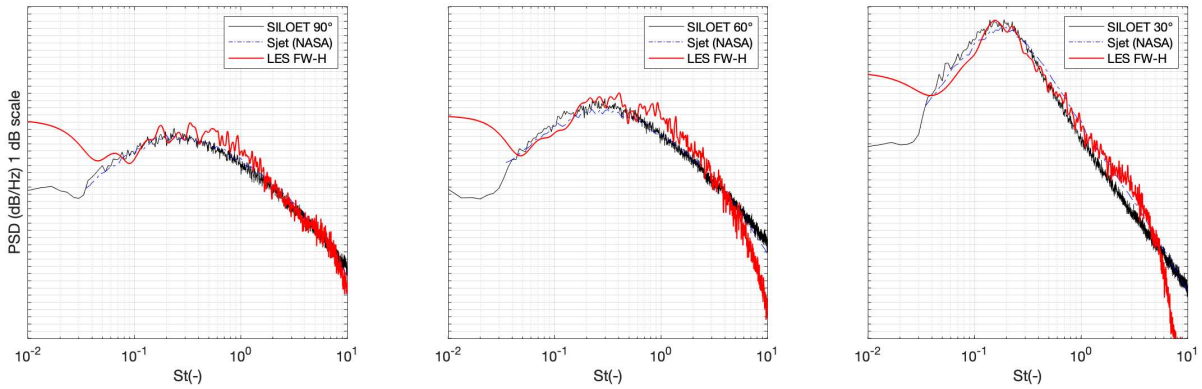

Fig. 3 LES-based noise spectra predictions for the cold SILOET jet experiment: comparison with the experiment and predictions of the empirical sJet model at 90º, 60º and 30º polar angles to the jet flow. The unit scale is 1dB/Hz.

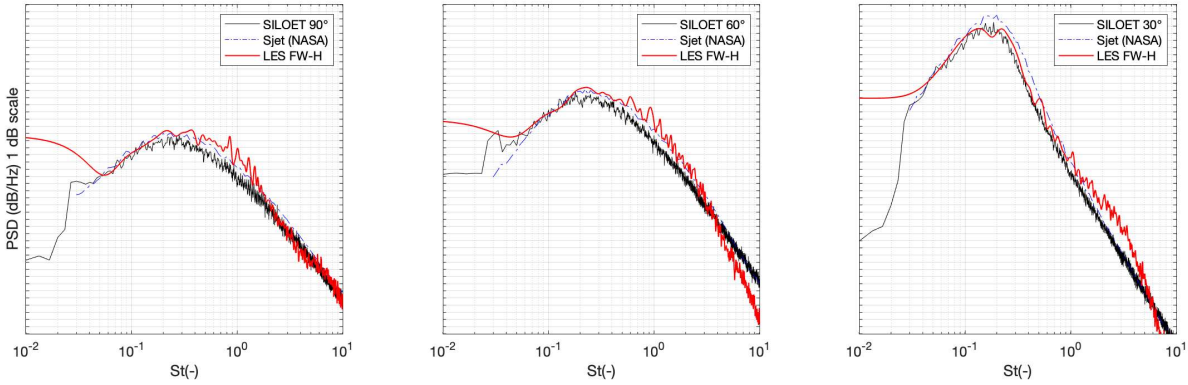

Fig. 4 LES-based noise spectra predictions for the hot SILOET jet experiment: comparison with the experiment and predictions of the empirical sJet model at 90º, 60º and 30º polar angles to the jet flow. The unit scale is 1dB/Hz.

The LES predictions are within 2dB from the experiment for most frequencies within $0.04 < St_D < 8$ for polar angles 30-90º, where St_D corresponds to the Strouhal number based on the nozzle exit diameter and the velocity at the nozzle exit. For very low frequencies, noise predictions are affected by the Welch averaging due to the shortness of the LES signal segments. There is also some minor overprediction of jet noise at high frequencies, which may be associated with the laminar inflow jet condition. Nevertheless, overall, for each jet case, the current LES solution is considered as a faithful representation of the high-speed turbulent jet flow for jet noise modelling purposes.

In addition, to test the acoustic model, the two NASA SHJAR jets corresponding to Set Point 3 and 7 conditions are considered, which details summarised in Table 2.

Table 2. The operating conditions of NASA SHJAR jet.

Set Point	M_a	T_j / T_0	NPR	M_j
3	0.5	0.950	2.297	0.513
7	0.9	0.835	2.861	0.985

The GPU LES solutions of the above NASA jets were previously obtained in [41], which will be used in the current work for acoustic modelling.

In addition to LES, RANS solutions of the same SILOET and NASA SHJAR jet cases are obtained. 3D-axisymmetric RANS equations are solved using the density-based solver in ANSYS Fluent. For spatial approximation on a body-fitted structured curvilinear grid, a second-order Roe flux-splitting scheme is selected. An implicit iterative scheme is used to converge the solution residuals within 10^{-5} of the initial values. Free inlet condition is imposed at the nozzle inlet in accordance with the jet operating conditions, and appropriate far-field conditions are imposed at the open downstream and lateral boundaries of the RANS domain. The total grid count of the RANS mesh is approximately $120 \cdot 10^3$ elements for all jets considered. The grid is iteratively refined near the nozzle wall boundary to reach the target dimensionless wall distance $y^+ \sim 1$ for the first off-the-wall grid cell. As discussed in [42], RANS turbulence models are not universal and their parameters are recommended to be calibrated in order to correctly capture the length of the jet potential core. For the current jet calculations, the $\kappa - \varepsilon$ RANS model with modified turbulence parameters suggested by [42] are used. Fig.5 shows a comparison of the RANS and LES solutions for the hot SILOET jet. It can be noted that the RANS solution is in a good agreement with the LES for the stream-wise component of the meanflow velocity. The agreement between RANS and LES for the turbulent kinetic energy is also reasonable. A similar level of agreement between RANS and LES is obtained for the cold SILOET and NASA jets. Notwithstanding the turbulence model calibration, the biggest advantage of RANS is its simplicity: its solution takes just a few hours to complete on a laptop per jet case.

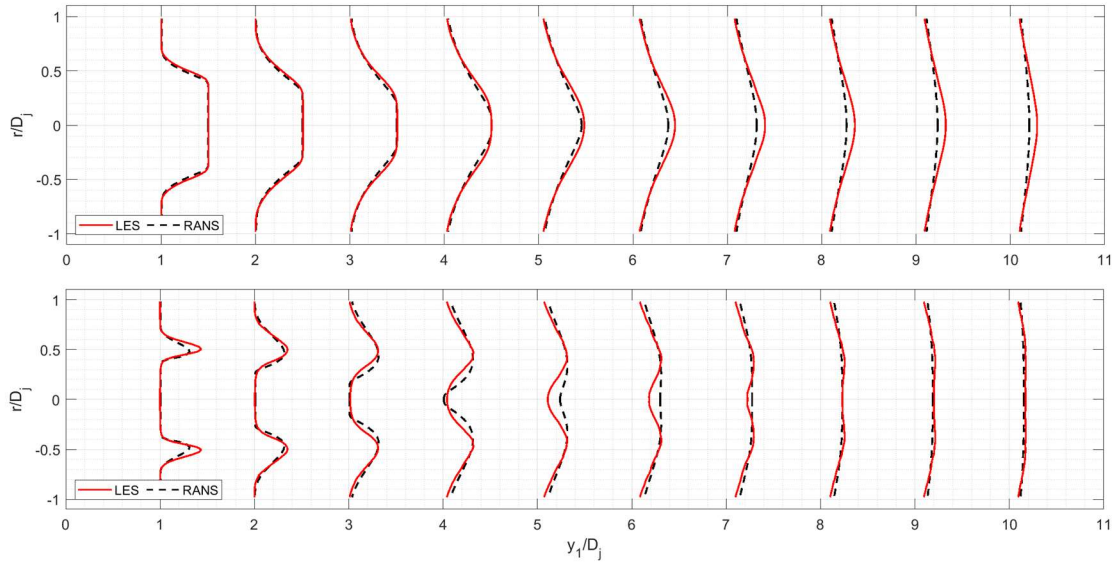

Fig. 5 Comparison of radial profiles of the mean axial velocity (top) and the turbulent kinetic energy (bottom) staggered in the stream-wise direction of the heated SILOET jet.

IV.Effective Source Modelling

The covariance of fluctuating Reynolds stresses in (11) are approximated by the Gaussian-exponential model following [8] and [18]

$$R_{ijkl}(\mathbf{y},\boldsymbol{\Delta},\tau)=A_{ijkl}(\mathbf{y})\exp\left[-\frac{|\Delta_1|}{\tilde{\nu}_1\tau_s}-\frac{\ln 2}{l_s^2}\left((\Delta_1-\tilde{\nu}_1\tau)^2+\Delta_2^2+\Delta_3^2\right)\right]. \tag{23}$$

As discussed in [5], the covariance of the fluctuating enthalpy term in (12) can be represented by a product of the velocity auto-correlation function and the fluctuating enthalpy intensity:

$$\hat{H}_{ij}(\mathbf{y},\boldsymbol{\Delta},\omega)=\hat{R}_{ij}(\mathbf{y},\boldsymbol{\Delta},\omega)\frac{\overline{h_t''^2}}{\widetilde{h^2}}, \tag{24}$$

The fluctuation of total enthalpy h_t' which comes in $\overline{h_t''^2}/\widetilde{h^2}$ is not available from RANS solutions directly, therefore following [43] the Empirical Temperature Variance model (ETV) is used. The fluctuating enthalpy intensity is further expressed as a function of the temperature gradient,

$$\overline{h_t^{'2}} / \widetilde{h^2} = F_T. \tag{25}$$

The empirical function of local temperature, F_T is defined as,

$$F_T = \left(\left| \frac{dT_t}{dr} \right| \frac{D_j}{T_\infty} \right)^{\zeta} \frac{(1-1/\mathrm{NTR})^{\delta}}{6} \chi, \quad \chi = \begin{cases} \chi_0 + (1-\chi_0)z, & z \le 1, \\ 1, & z > 1, \end{cases} \tag{26}$$

where $z = x / L_c$, where L_c is the length of the potential core of the jet, $\zeta = 0.2$, $\chi_0 = 0.7$, $\delta = 1 + 1/(3\mathrm{NPR})$ and NTR and NPR are the nozzle temperature ratio and the nozzle pressure ratio parameters, respectively. Notably, the fluctuating enthalpy intensity function, F_T, which scales as the temperaure gradient, is negligible for the cold SILOET jet case in comparison with the hot jet case.

As a consistency check, the root-mean-square (r.m.s) of the enthalpy fluctuations (the enthalpy source strength) available from the LES solution can be compared with the ETV function F_T for the hot jet case. Fig.6 shows the distributions of ETV function obtained from RANS and LES mean flow fields and the enthalpy source strength extracted from LES solution. Notably, the LES and RANS solutions of the ETV function are in good agreement with each other. They are also in a reasonable agreement with the enthalpy source strength computed directly from LES.

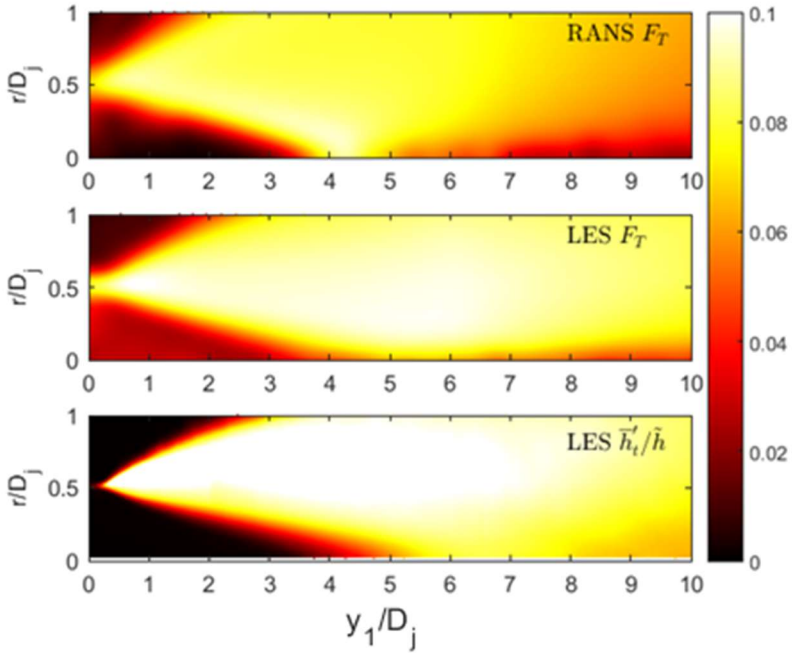

Fig. 6 Distributions of the ETV function in the hot SILOET jet flow: RANS (top) and LES (middle) solutions; the enthalpy source strength extracted from LES is shown at the bottom.

The velocity co-variance

$$R_{ij}(\mathbf{y},\Delta,\tau)=\overline{v'_i(\mathbf{y},t)v'_j(\mathbf{y}+\Delta,t+\tau)}\,, \tag{27}$$

which appears in (24), is approximated using the Gaussian-exponential model

$$R_{ij}(\mathbf{y},\Delta,\tau)=A_{ij}(\mathbf{y})\exp\left[-\frac{|\Delta_1|}{\tilde{v}_1\tau_s}-\frac{\ln 2}{l_s^{\,2}}\left((\Delta_1-\tilde{v}_1\tau_s)^2+\Delta_2{}^2+\Delta_3{}^2\right)\right]. \tag{28}$$

by analogy with modelling the co-variance of the fluctuating Reynolds stresses (22).

By substituting (23) and (24) in the far-field acoustic integral expressions (11) and (12), where the locally parallel adjoint Green's function solution is used together with the assumption about the radially compact correlation scales. Following [8, 18], the so-called compact source approximation, i.e. neglecting the radial variation of Green's function and its derivatives in (15) over the correlation length of turbulent sources is made. It was shown in [18] that this approximation is reasonable upstream of the end of the potential core of the jet, where the shear layers are relatively thin for a range of acoustic wavelengths of interest.

Using the above assumptions, the double integrals (11), (12) reduce to a single integration over the jet volume,

$$S^{(\mathrm{cold})}=\int_V\int_V A_{ijkl}(\mathbf{y})W(\mathbf{y})\hat{I}_{ij}\hat{I}^*_{kl}d\mathbf{y},\ \text{and}\ S^{(\mathrm{hot})}=\int_V\int_V A_{ij}(\mathbf{y})W(\mathbf{y})\hat{I}_i\,\hat{I}^*_j d\mathbf{y}, \tag{29}$$

where the function $W(\mathbf{y})$, which emerges as a result of the analytical integration over the correlation volume Δ, is:

$$W(\mathbf{y})=\left(\frac{\pi}{\ln 2}\right)^{3/2}\frac{2l_s^3\tau_s}{1+(\omega(1-\tilde{v}_1/c_\infty\cos\varphi)\tau_s)^2}\exp\left(-\frac{(\omega l_s/\tilde{v}_1)^2}{4\ln 2}\right). \tag{30}$$

Following [5], the amplitudes of the co-variances of the Reynolds stresses and the enthalpy terms are modelled via the time-averaged quantities, such as the turbulent kinetic energy, κ, which is readily available from both LES and RANS models, and also the fluctuating enthalpy intensity,

$$A_{ijkl}(\mathbf{y}) = C_{ijkl}(2\overline{\rho}\kappa)^2, \quad A_{ij}(\mathbf{y}) = C_{ij}\rho_\infty c_\infty^4 \overline{\rho}\kappa F_T. \tag{31}$$

For each jet case, the dimensionless coefficients C_{ijkl} and C_{ij} in Eq.(29) are computed from the LES solution in the shear layer location corresponding to the nozzle lip-line $(r / D_j = 0.5)$ as follows:

- Calculate amplitudes of the covariance terms, which correspond to several major components; average them in the azimuthal direction to obtain $R_{ijkl}(y_1)$ and $R_{ij}(y_1)$ as functions of the stream-wise coordinate, y_1 only.
- Non-dimensionalise the computed amplitudes by the maximum value of the stream-wise components,

$$\alpha_{ijkl}(y_1) = \frac{R_{ijkl}(y_1)}{\max(R_{1111})}, \quad \beta_{ij}(y_1) = \frac{R_{ij}(y_1)}{\max(R_{11})},$$

  which distributions are shown in Figs.7 and 8 for the cold and hot jets, respectively. In particular, it can be noted that the most important Reynolds stress covariance correspond to the stream-wise term R_{1111} (and a similar term for the velocity covariance) while the cross-stream term $R_{r\theta r\theta}$ appears to be least prominent.
- Average the non-dimensionalised amplitudes $\alpha_{ijkl}(y_1)$ and $\beta_{ij}(y_1)$ over the jet stream-wise coordinate in the vicinity of the end of the jet potential core (y_{c1} / D_j = 4-6, where the potential core length, y_{1c} is defined as the distance from jet nozzle exit to the axial location, where the time-averaged velocity first drops below 99% of the jet velocity at the nozzle exit) to obtain $\langle \alpha_{ijkl} \rangle$ and $\langle \beta_{ijkl} \rangle$, which values are summarised in Tables 3 and 4.
- Normalise the amplitudes of the stream-wise correlation components on the turbulent kinetic energy at the stream-wise location $y_1 = y_{1c}$,

$$\alpha_0 = \frac{R_{1111}}{(2\bar{\rho}\kappa)^2}, \quad \beta_0 = \frac{R_{11}}{\bar{\rho}\kappa},$$

which parameters for both the SILOET jets are found to be close to unity.

- Finally compute the non-dimensional amplitudes coefficients C_{ijkl} and C_{ij} to be used in Eq.(30),

$$C_{ijkl} = \langle \alpha_{ijkl} \rangle \alpha_0, \quad C_{ij} = \langle \beta_{ij} \rangle \beta_0.$$

Notably, the relative magnitudes of the different components were computed from the LES solution rather than resorting to the isotropy assumption typical of the 'fine-scale noise' model [8]. Furthermore, it was previously discussed in [18] that only 6 dominant amplitude components give the largest contribution to the predicted spectrum, as the relative amplitudes of other components are small. In case of the fourth-order velocity correlation function, the most dominant are axial R_{1111}, radial R_{rrrr} and circumferential $R_{\theta\theta\theta\theta}$ terms. In addition, cross terms R_{1r1r}, $R_{1\theta1\theta}$ and $R_{r\theta r\theta}$ (and the components equal to them from the symmetry) are also significant (Fig.7a,8a). In comparison with this, the second-order correlations have only 3 dominant components of Cartesian directions (Fig7b,8b).

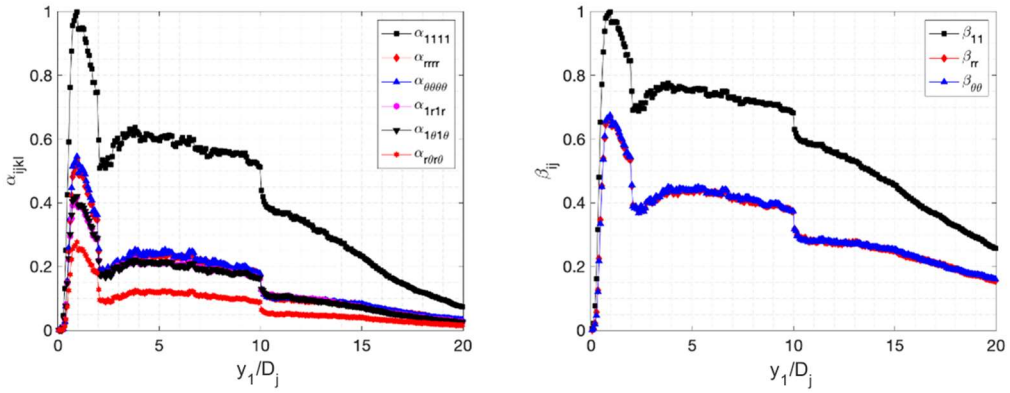

(a) (b)

Fig. 7 Lipline distributions of the dimensionless amplitudes of the covariance of fluctuating Reynolds stresses (a) and velocity fluctuations (b) along the jet lipline for the cold SILOET jet.

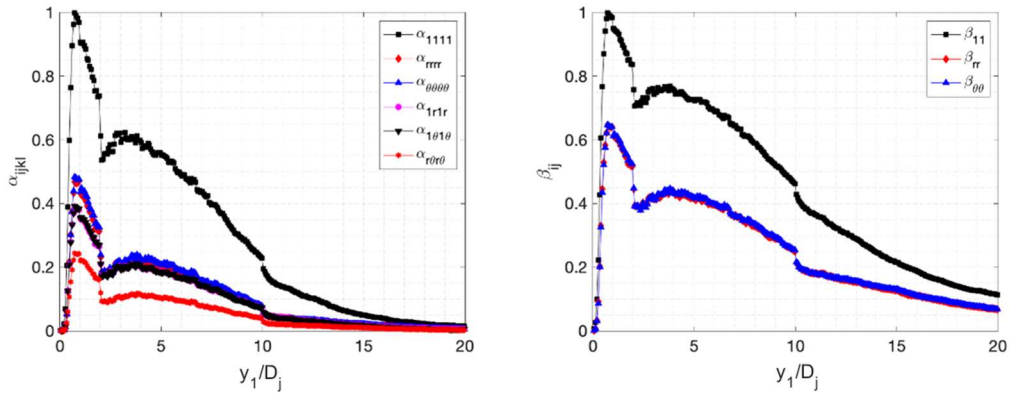

(a) (b)

Fig. 8 Lipline distributions of the dimensionless amplitudes of the covariance of fluctuating Reynolds stresses (a) and velocity fluctuations (b) along the jet lipline for the hot SILOET jet.

Table 3. Non-dimensional quadrupole source amplitudes

$\langle \alpha_{ijkl} \rangle$	11,1 1	rr, rr	$\theta\theta, \theta\theta$	$1r, 1r$; $1r, r1$; $r1, 1r$; $r1, r1$;	$1\theta, 1\theta$; $1\theta, \theta1$; $\theta1, 1\theta$; $\theta1, \theta1$	$r\theta, r\theta$; $1\theta, 1\theta$; $\theta r, r\theta$; $\theta r, \theta r$
cold	1	0.355	0.360	0.327	0.326	0.180
hot	1	0.360	0.369	0.329	0.331	0.183

Table 4. Non-dimensional dipole source amplitudes

$\langle \beta_{ij} \rangle$	11	rr	$\theta\theta$	$1r$	1θ	$r\theta$
cold	1	0.586	0.330	0.331	0	0
hot	1	0.453	0.257	0.259	0	0

To close the model (23), (27), and (28), the acoustic correlation scales, l_s , τ_s are required for each point of the jets. However, as it was pointed out in [22], the calculation of the acoustic length scales in the entire jet volume from the first principles, e.g. using the definition from Eqs.(14), is too laborious to perform

directly and accurate interpolation of these quantities are not straightforward. Hence, following [5], [8], [17] the space and time length scales are computed from the time-averaged turbulent kinetic energy and dissipation rate,

$$l_s = c_\ell \kappa^{1.5} / \varepsilon,\ \tau_s = c_\tau \kappa / \varepsilon. \tag{32}$$

The two dimensionless parameters, c_l and c_τ are determined by fitting the shape and the amplitude of the model spectrum to the far field noise data for each SILOET jet at the observer angle at 90° observer angle (and then kept fixed for all other observer angles).

For the sake of simplicity of the model, the same dimensionless length scale parameters of the fourth-order and the second-order velocity correlation functions will be assumed despite the experimental and computational evidence suggesting that these scales are different. These dimensionless length scale parameters c_l and c_τ are effectively treated as empirical parameters of the global fit. The sensitivity of the acoustic model results to the empirical fit parameters and the degree of universality of these parameters for different jets is another important contribution of the current paper.

In comparison with the turbulent kinetic energy, the calculation of the turbulence dissipation rate from LES using the quadratic form of the turbulent velocity strain rate [44] is challenging since the instantaneous strain rate is a very noisy quantity. Hence, following the standard RANS-like modelling assumption, the turbulence dissipation from LES is calculated by assuming equilibrium of the turbulence dissipation and production terms.

Still, it can be argued that the RANS-like equilibrium assumption conflicts with the LES principle of having large eddies explicitly resolved in the simulation, which makes the resulting LES-based acoustic model less consistent (and less accurate as will be shown in Section V). Hence, in addition to the acoustic scale model (32), the second approach is suggested, which combines the turbulent kinetic energy with the time-averaged absolute vorticity solution component,

$$l_s = c_\ell \sqrt{\kappa} / \xi,\ \tau_s = c_\tau / \xi, . \tag{33}$$

Notably, in comparison with the turbulence dissipation rate, the time-averaged absolute vorticity is a well-defined quantity for both the LES and RANS solutions.

Table 5 summarises the dimensionless parameters resulting c_l and c_τ corresponding to models (32) and (33) for LES and RANS flow solutions of the cold and hot SILOET jets.

Table 5. Acoustic length and time scale coefficients for the cold and hot SILOET jet cases

Model		Eq.(32)		Eq.(33)	
		c_l	c_τ	c_l	c_τ
RANS-based	Cold SILOET jet	0.496	0.313	1.396	1.433
	Hot SILOET jet	0.416	0.293	1.965	1.100
LES-based	Cold SILOET jet	0.695	0.550	2.190	1.965
	Hot SILOET jet	0.586	0.303	1.965	1.100

V. Results of the acoustic modelling

Figs. 9 and 10 show the results of the far-field noise Power Spectral Density (PSD) predictions using the generalised acoustic analogy models based on the LES and RANS flow solutions of cold and hot SILOET jets, where the acoustic scale model (32) is used. It can be seen that both predictions capture the noise spectra within 2dB for polar angles 60 ° and 90° and the frequency range $0.03 < St_D < 3$. For 30° observer angle, both the LES and the RANS-based models tend to over amplify the noise at frequencies lower than $St_D = 0.2$ corresponding to the peak jet noise in the experiment. The low-frequency noise amplification is especially notable for the LES-based acoustic analogy model of the hot jet. For the same shallow observer angle, the noise spectra of the LES solutions for both the cold and hot jets show a shift of the peak noise frequency from $St_D = 0.2$ to $St_D = 0.1$-0.15. The RANS-based acoustic model predictions are

accurate within 2dB for the frequency range $0.05 < St_D < 3$. In comparison to these, the range of 2dB accuracy of the LES model at low frequencies is limited to $St_D = 0.08\text{-}0.1$, which limitation can be related to the inconsistency of turbulence dissipation rate definition for large eddies in LES. In comparison with the problems at low frequencies, the same LES-based acoustic model captures the high-frequency part of the noise spectra ($St_D > 0.2$) at 30º polar angle within 1 dB from the experiment up to $St_D = 4$.

Figs. 11 and 12 show the results of the far-field noise PSD predictions using the same the LES and RANS flow solutions, where the alternative acoustic scale model Eq.(33) is used, which involves the time-averaged vorticity magnitude instead of the turbulence dissipation rate. In this case, the low-frequency noise predictions of the LES-based acoustic model are notably improved especially in comparison with the previous hot jet spectrum solution (Fig.10c). For this acoustic scale model, the range of accuracy of the LES-based noise predictions extends to low frequencies, $St_D = 0.05\text{-}0.06$. For both the cold and the hot jet, the noise spectra predictions of the LES-based model using the mean vorticity acoustic scales are consistently within 2dB from the experiment in the frequency range of $0.06 < St_D < 0.2$ and 1 dB for higher frequencies, $0.2 < St_D < 4$.

In comparison with the favorable effect of choosing the mean vorticity solution component for the acoustic scale calculation of the LES-based model, the predictions of the RANS-based model based on the mean vorticity solution are less accurate. The RANS model based on the acoustic scales defined (33) is within 2-3dB from the experiment for the frequency range $0.05 < St_D < 4$. This suggests that the conventional definition of the acoustic scales based on the turbulence kinetic energy and dissipation rate, as originally proposed by [8] is the best choice for RANS-based acoustic analogy models of jet noise.

It can also be noted that all four considered acoustic analogy models (the LES- and RANS- based models with the acoustic scales defined by (32) and (33)) are more accurate for predicting the high-frequency noise spectra (e.g. $St_D > 0.3$) for the hot jet case (Figs.10, 12) in comparison with the cold jet. This is especially evident for larger observer angles, 90º and 60º (comp. Figs.9a,b with Figs.10a,b and Figs.11a,b with Figs.12a,b). The difference in model accuracy for high-frequency noise can be explained by thicker initial

shear layers of the hot jet, which corresponds to a lower Reynolds number in comparison with the cold jet. The thicker shear layers make the hot jet flow more amenable for the LES solution, which is used to obtain the covariance of fluctuating Reynolds stresses and the velocity autocorrelation.

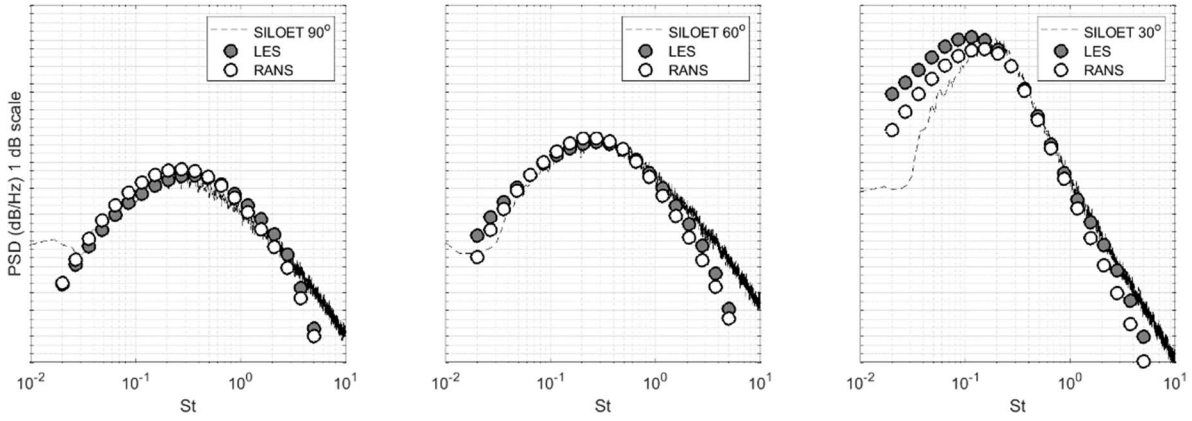

(a) (b) (c)

Fig. 9 Noise spectra predictions of the cold SILOET jet case: comparison of the LES- and RANS-based models based on the acoustic scales defined by Eq.(32) with the experiment for 90°, 60°, and 30° observer angle.

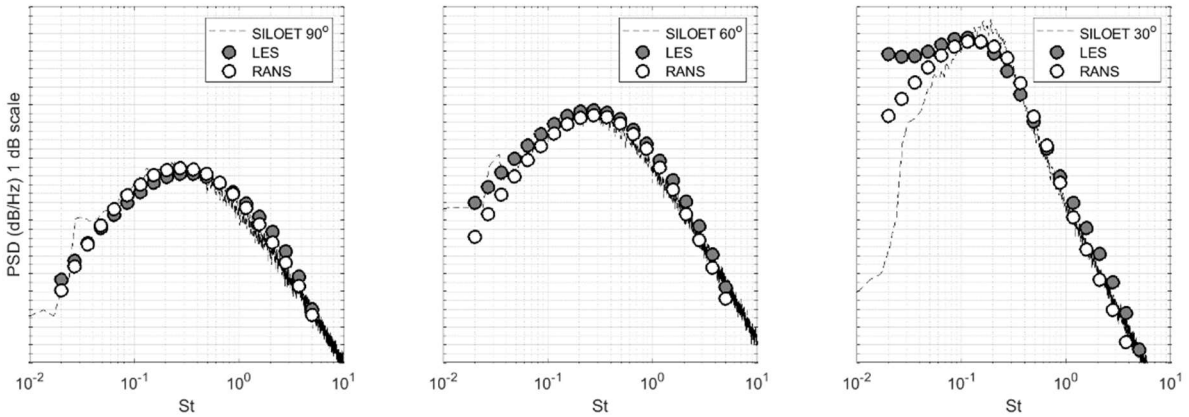

(a) (b) (c)

Fig. 10 Noise spectra predictions of the hot SILOET jet case: comparison of the LES- and RANS-based models based on the acoustic scales defined by Eq.(32) with the experiment for 90°, 60°, and 30° observer angle.

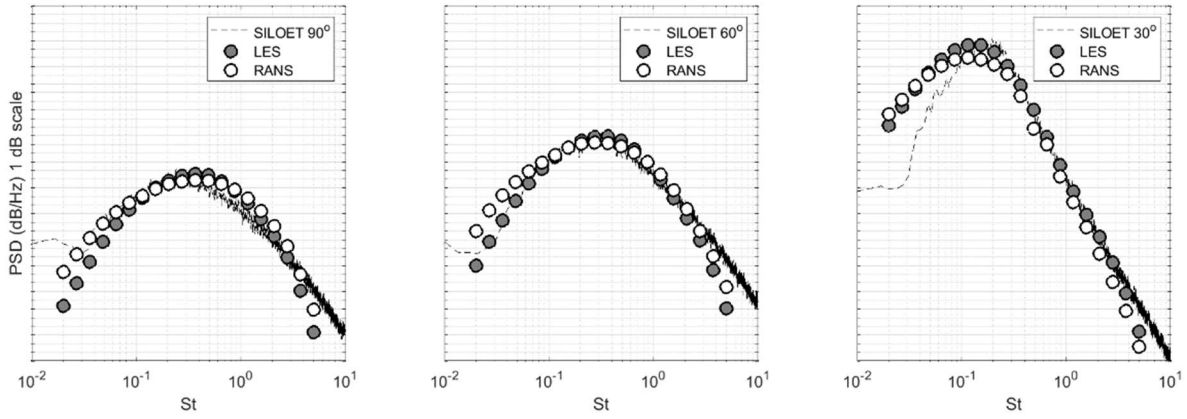

(a) (b) (c)

Fig. 11 Noise spectra predictions of the cold SILOET jet case: comparison of the LES- and RANS-based models based on the acoustic scales defined by Eq.(33) with the experiment for 90º, 60º, and 30º observer angle.

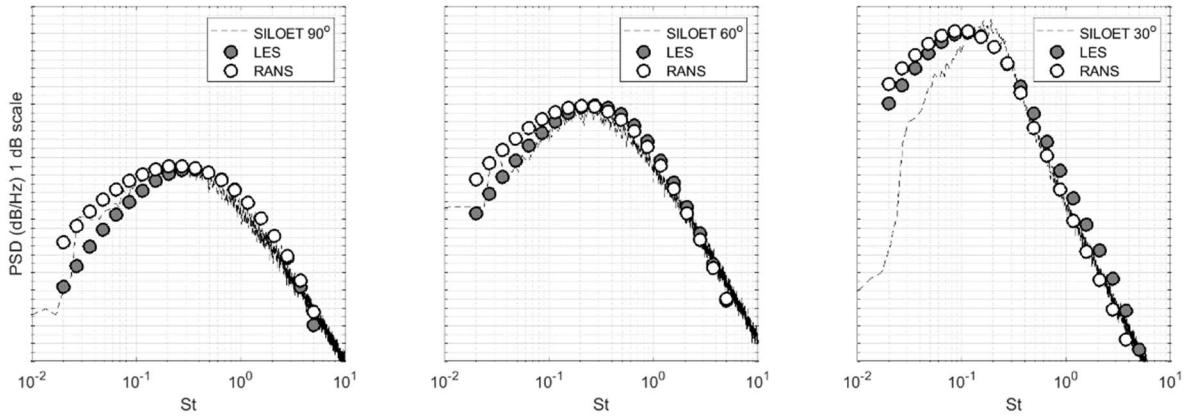

(a) (b) (c)

Fig.12 Noise spectra predictions of the hot SILOET jet case: comparison of the LES- and RANS-based models based on the acoustic scales defined by Eq.(33) with the experiment for 90º, 60º, and 30º observer angle.

As the next step in the verification of the suggested acoustic model, the set of dimensionless space and time length scale parameters computed for the hot SILOET jet (Table 5) are substituted in the acoustic

model of the cold SILOET jet to probe the sensitivity of the jet noise spectra predictions to these empirical coefficients.

The Figs.13-14 compare the far-field noise prediction of cold SILOET jet using both sets of the acoustic scale parameters (Table 5). Notably, the RANS-based acoustic model using the conventional definition of acoustic length and time scales (32) shows a consistent 2-3dB accuracy in comparison with the experiment for both sets of the acoustic scale parameters. In a similar way, for the LES-based model using the time-averaged vorticity (33) also shows a low sensitivity to the calibration parameters and a 2-3dB agreement with the experiment for all observer angles. In contrast to this, both the RANS-based acoustic model using the time-averaged vorticity scale and the LES-based model using the conventional acoustic scale definition lead to a poor agreement with the experiment.

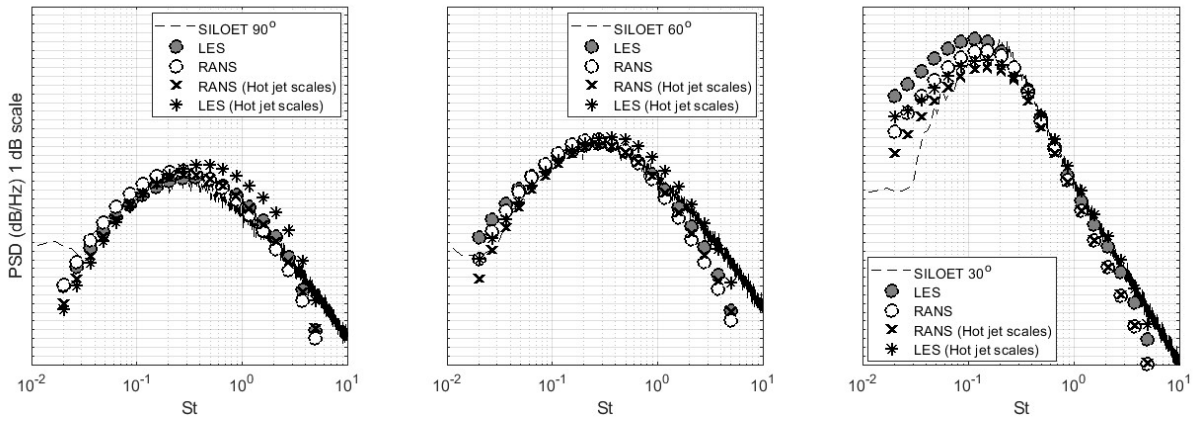

(a) (b) (c)

Fig.13 Sensitivity of the noise spectra predictions of the cold SILOET jet to the acoustic length scale parameters: comparison of the LES- and RANS- based models based on the acoustic scales defined by Eq.(32) with the experiment for 90°, 60°, and 30° observer angle.

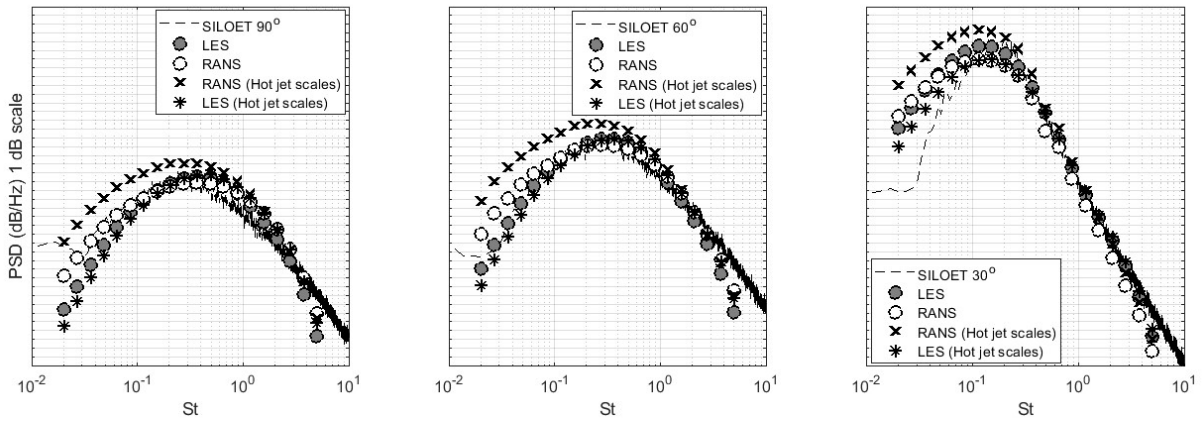

(a) (b) (c)

Fig.14 Sensitivity of the noise spectra predictions of the cold SILOET jet to the acoustic length scale parameters: comparison of the LES- and RANS- based models based on the acoustic scales defined by Eq.(33) with the experiment for 90º, 60º, and 30º observer angle.

Finally, to test thegenerality of the dimensionless coefficients of the suggested acoustic model, the dimensionless space and time length scale coefficients (Table 5) as well as the relative amplitude parameters (Table 3) corresponding to the cold SILOET jet are applied to the far-field noise predictions of the two NASA SHJAR jets (Table 2). Importantly, the LES and RANS solutions of the NASA jets are used in the same way to provide simple time-averaged flow and turbulence quantities rather than the fourth-order velocity correlation functions. The resulting spectra predictions of the acoustic model are shown in Figs.15-18 for both the methods of the acoustic length scale definitions, (32) and (33). In all cases, the dimensionless coefficients of the acoustic model obtained for the cold SILOET jet work well for the NASA SHJAR jets including the acoustic Mach number 0.5, which is 55% smaller compared to the SILOET jet (acoustic Mach number 0.875).

Consistently with the previous results, the LES-based acoustic model shows an improved accuracy for the alternative acoustic scale definition (33) in comparison with (32) leading to 2-3dB agreement with the experiment upto St_D = 2-3 while capturing the peak noise within 1dB (Figs.17 and 18).

Following the same trend, the RANS-based acoustic model remains most robust for the conventional definition of length and time scales (32) with capturing the peak noise within 1 dB (Figs. 15 and 16) while underpredicting high-frequency noise compared to the best LES-based model (Figs. 17 and 18). Interestingly, for the Mach 0.5 NASA jet, the RANS-based acoustic model based on the meanflow vorticity (33) leads to surprisingly good predictions including high frequencies, almost as good as those of the LES-based model (Fig.17). However, the same is not true for the high-speed NASA jet case (Fig.18). We attribute the larger sensitivity of the RANS-based model to the acoustic parameters to the fact that the RANS flow solution is less accurate compared to the LES solution

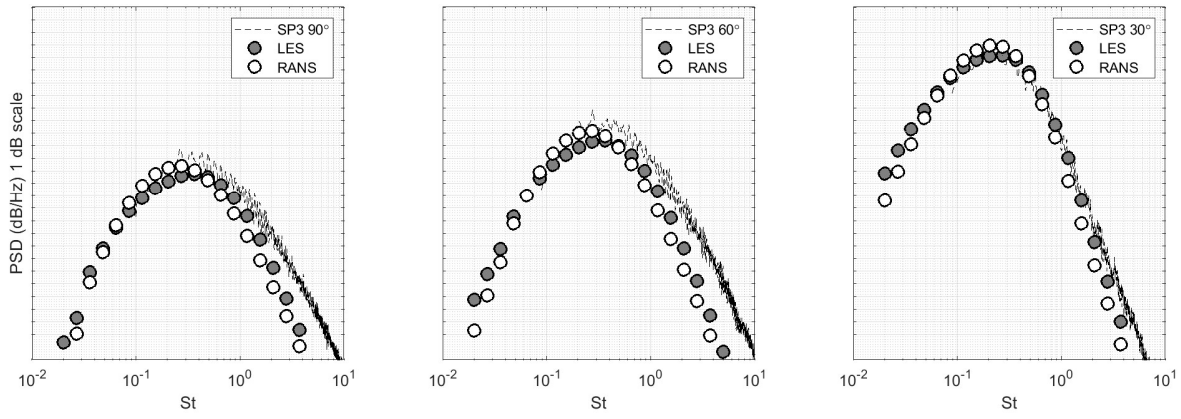

(a) (b) (c)

Fig.15 Noise spectra predictions of the NASA SHJAR jet for SP3 case: comparison of the LES- and RANS- based models based on the acoustic scales defined by Eq.(32) with the experiment for 90º, 60º, and 30º observer angle.

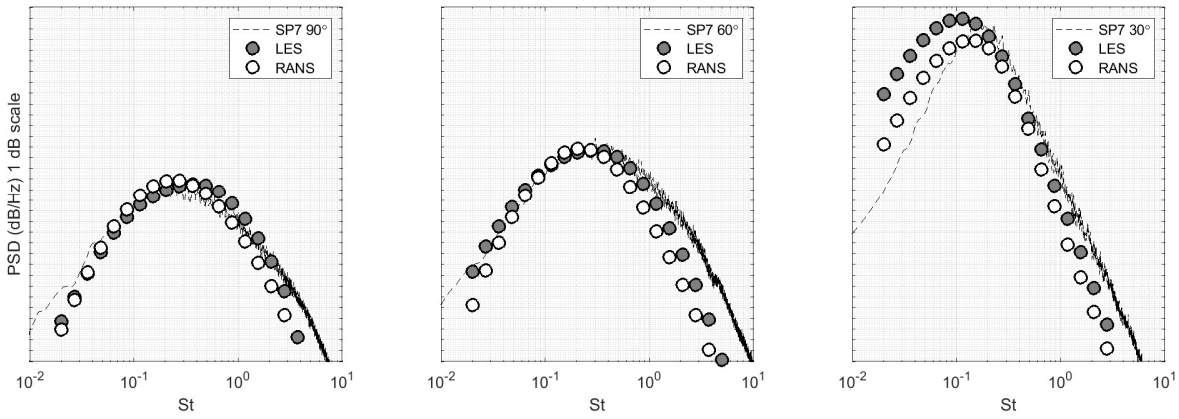

(a) (b) (c)

Fig.16 Noise spectra predictions of the NASA SHJAR jet for SP7 case: comparison of the LES- and RANS- based models based on the acoustic scales defined by Eq.(32) with the experiment for 90º, 60º, and 30º observer angle.

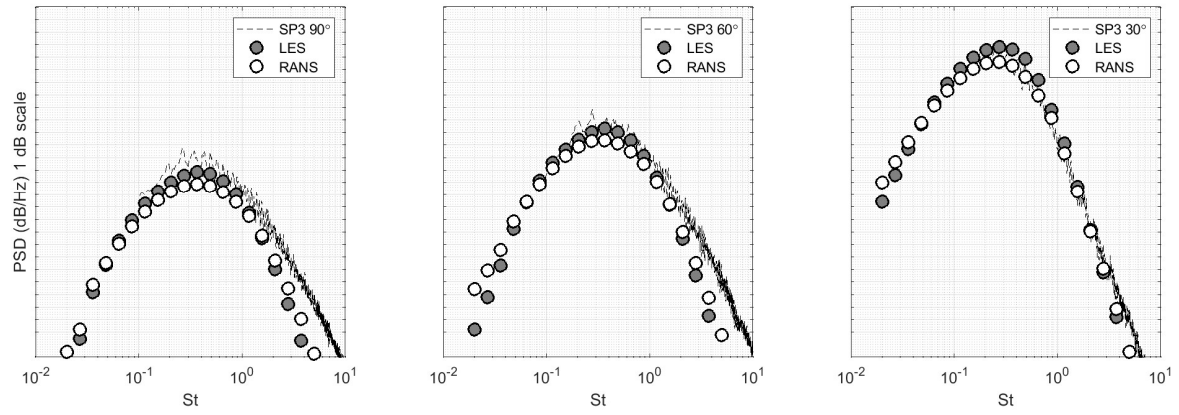

(a) (b) (c)

Fig.17 Noise spectra predictions of the NASA SHJAR jet for SP3 case: comparison of the LES- and RANS- based models based on the acoustic scales defined by Eq.(33) with the experiment for 90º, 60º, and 30º observer angle.

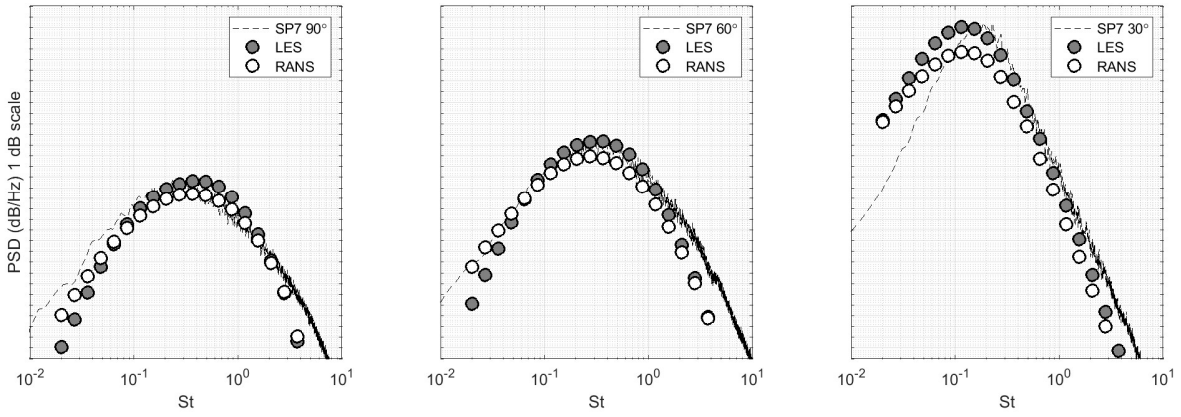

(a) (b) (c)

Fig.18 Noise spectra predictions of the NASA SHJAR jet for SP7 case: comparison of the LES- and RANS- based models based on the acoustic scales defined by Eq.(33) with the experiment for 90º, 60º, and 30º observer angle.

VI. Conclusion

Goldstein Generalised Acoustic Analogy models are implemented for the hot and cold static high-speed jet cases at the same acoustic Mach number corresponding to conditions of the SILOET experiment performed by QinetiQ. Following [20], the models are based on the validated Large Eddy Simulation (LES) solutions from which the covariances of fluctuating Reynolds stresses are computed. In addition, following [5], the suggested models ignore the correlation between the fluctuating Reynolds stresses and the fluctuating enthalpy fluctuation terms. The empirical model suggested by Khavaran and Bridges [43] is used to approximate the covariance of fluctuating enthalpy sources as a product of the velocity covariance and a function of the local temperature gradient in the jet. Importantly, the latter function is free from tuneable parameters and automatically tends to zero in the cold jet where the temperature gradient is negligible. Similar to the covariances of the fluctuating Reynolds stresses, the relative amplitudes of the velocity autocorrelations are computed from LES for both the jet cases.

The LES-based implementation of the Goldstein generalised acoustic analogy together with the Khavaran and Bridges model for hot jet noise predictions is one important contribution of this paper.

Inputs to the suggested acoustic models include single-point quantities such as the time-averaged local stream-wise velocity, sound speed, temperature, vorticity magnitude, turbulent kinetic energy, and dissipation rate. All these quantities are extracted from the LES and a separate Reynolds Averaged Navier Stokes (RANS) solution, which is cross-validated in comparison with the LES solution. Two tuneable parameters of the suggested acoustic models correspond to the acoustic correlation length and time scales, which require additional approximations in the context of low-order modelling. The first acoustic-scale model is based on using the turbulence scales associated with the turbulent kinetic energy and dissipation rate in accordance with recommendations in the jet noise literature [8]. The second model is derived by replacing the turbulent energy dissipation rate with the time-averaged absolute vorticity, which is another novel contribution of the current work. Notably, in comparison with the turbulent energy dissipation rate, the mean vorticity can be consistently computed from the LES solution.

The choice of using the turbulent energy dissipation rate in the definition of the acoustic scales is considered first. Both the LES and the RANS acoustic models based on the turbulent energy dissipation rate are within 2dB from the experimental spectra for polar angles 60 ^{o} and 90^{o} and the frequency range $0.03 < St_D < 3$. For 30^{o} observer angle, the LES- and the RANS-based solutions tend to over amplify noise at frequencies lower than $St_D = 0.2$ corresponding to the peak jet noise in the experiment. For the RANS-based model, the amplification is moderate: the spectra predictions are within 2 dB from the experiment for the frequency range $0.05 < St_D < 3$. The low-frequency noise amplification is especially notable for the LES-based acoustic model of the hot jet. The noise spectra of the LES solutions for both the cold and hot jets show a shift of the peak noise frequency from $St_D = 0.2$ to $St_D = 0.1$-0.15. The model accuracy cut-off at low frequencies corresponds to $St_D = 0.08$-0.1. The loss of accuracy of the LES-based model at low frequencies is explained by the RANS-like assumption used in the calculation of turbulent energy dissipation rate, which is not consistent with large eddies of the LES solution. On the other hand, the LES-based acoustic model captures the high-frequency part of the noise spectrum at 30^{o} polar angle very accurately (within 1 dB) up to frequencies $St_D = 4$.

The choice of using the time-averaged local vorticity in the definition of the acoustic scales is considered next. In this case, the low-frequency noise predictions of the LES-based acoustic model are notably improved especially for the hot jet noise spectrum at 30°, which may suggest that the RANS-like assumption works less good in the hot jet. For the vorticity-based acoustic scale model, the range of accuracy of the LES-based noise predictions extends to lower frequencies, St_D = 0.05-0.06. For both the cold and the hot jet, the noise spectra predictions of the LES-based model are consistently within 2 dB from the experiment in the frequency range of 0.06 < St_D < 0.2 and 1 dB for higher frequencies, 0.2 < St_D <4. In comparison with the favorable effect of choosing the mean vorticity solution component for the acoustic scale calculation of the LES-based model, the predictions of the RANS-based model based on the mean vorticity solution are less accurate. The RANS-based model noise spectra predictions are within 2-3dB from the experiment for frequencies 0.05 < St_D < 4. The latter suggests that the conventional definition of the acoustic scales based on the turbulence kinetic energy and dissipation rate [8], is the best choice for RANS-based acoustic analogy models of jet noise.

All four considered acoustic analogy models are more accurate for predicting the high-frequency noise spectra (e.g. St_D > 0.3) for the hot SILOET jet in comparison with the cold SILOET jet. The difference in model accuracy for high-frequency jet noise can be attributed to the thicker initial shear layers of the hot jet, which corresponds to a lower Reynolds number in comparison with the cold jet. The thicker shear layers make the hot jet flow more amenable for the LES solution, which is used to obtain the covariance of fluctuating Reynolds stresses and the velocity autocorrelation for all models.

One limitation of the suggested hot jet noise model is the use of the empirical dimensionless length scale parameters corresponding to acoustic space and time scales. Instead of deriving these parameters by computing the acoustic scales from the high-order statistics of the local turbulent jet flow, they are obtained using a global fit to the reference far-field noise spectrum at 90° observer angle. While this leads to a significant simplification of the implemented GAA model, it also raises a question how universal the derived empirical length scale parameters are. Hence, a series of additional model sensitivity investigations

is performed, which include: (i) substitution of the acoustic length and time scale coefficients derived for hot SILOET jet flow to the acoustic model for the cold SILOET jet and (ii) substitution of the dimensionless acoustic scales and relative amplitude coefficients derived for the cold SILOET jet to the acoustic models of the NASA SHJAR jets corresponding to Set Points 3 and 7. In all cases it is shown that the LES-based model using the meanflow vorticity acoustic definition and the RANS-based model using the conventional dissipation rate acoustic scale definition are able to capture noise within 2-3dB from the experiment for a good range of frequencies upto St_D = 2-3 and observer angles while capturing the peak noise within 1dB. The RANS-based predictions show somewhat more sensitivity to the acoustic model parameters, which is attributed to less accuracy of the RANS flow solution compared to the LES for some of the jet flows considered.

The robustness of the implemented GAA model with respect to the empirical acoustic scale calibration parameters suggests that its validity range is reasonably large. Once calibrated for a class of single-stream hot jet flows using LES, the suggested acoustic low-order model purely based on RANS can be efficiently used for a range of cold and hot jet noise predictions without any further LES input in a multi-fidelity design optmisation loop.

Acknowledgement

The authors are grateful to the UK Government for supporting the SILOET program (Innovate UK (former TSB), Reference number 110032) during which the model-scale data was acquired in the QinetiQ NTF and Dr Paul Strange (Rolls-Royce Plc) for facilitating access to these data.

The work of A.P. Markesteijn and S.A. Karabasov have been supported by the Engineering and Physical Sciences Research Council (EP/S002065/1), and S.A. Karabasov has been further supported by the Russian Science Foundation (Grant Nos. 19-12-00256 and 21-71-30016).

The authors thank Abbas Khavaran for making his sJet code readily available.

Reference List

[1] Morfey, C. L., Szewczyk, V.M., Tester, B. J., "New scaling laws for hot and cold jet mixing noise based on geometric acoustics model," *Journal of Sound and Vibration,* Vol. 61(2), pp. 255-292, 1978. https://doi.org/10.1016/0022-460X(78)90007-X.

[2] Tam, C.K., Pastouchenko, N. N., Viswanathan, K., "Fine-Scale Turbulence Noise from Hot Jets", *AIAA Journal.* Vol. 43, No. 8 (2005), pp. 1675-1683. https://doi.org/10.2514/1.8065.

[3] Viswanathan, K., "Aeroacoustics of hot jets," *Journal of Fluid Mechanics*, 516, pp. 39-82, 2004. doi:10.1017/S0022112004000151.

[4] Musafir, R. E., "Relating far field noise spectra of cold and hot jets," *Proceedings of 13th International Congress of Sound and Vibration*, Vienna, 2006.

[5] Khavaran, A., Kenzakowski, D.C., Mielke-Fagan, A.F., "Hot jets and sources of jet noise," *International Journal of Aeroacoustics,* Vol. 9 pp. 491-532. https://doi.org/10.1260/1475-472X.9.4-5.491.

[6] Biolchini, R., Daviller, G., Bailly, C., Bodard, G., "Temperature effects on the noise source mechanisms in a realistic subsonic dual-stream jet," *Computers & Fluids,* Vol. 213, 1047200, 2020. https://doi.org/10.1016/j.compfluid.2020.104720.

[7] Tam, C.K., Chen, K.C., "A statistical model of turbulence in two-dimensional mixing layers," *Journal of Fluid Mechanics*. Vol. 92, 303-326, 1979. https://doi.org/10.1017/S002211207900063X.

[8] Tam, C. K. W., Auriault, L., "Jet Mixing Noise from Fine-Scale Turbulence," *AIAA Journal*, Vol. 37, No. 2, pp.145-153, 1999.

[9] Jordan, P., Colonius, T., "Wave Packets and Turbulent Jet Noise," *Annual Review of Fluid Mechanics*. Vol. 45. pp. 173-195, 2013. https://doi.org/10.1146/annurev-fluid-011212-140756.

[10] Lighthill, M.J., "On sound generated aerodynamically: I. General Theory." *Proceedings of The Royal Society of London*, Vol. 211,1952, pp. 564-587. https://doi.org/10.1098/rspa.1952.0060.

[11] Lilley, G.M., "On the noise from jets, Noise Mechanisms," AGARD-CP-131, 13.113.12, 1974.

[12] Ffowcs Williams, J. E., "The noise from turbulence convected at high speed," *Philosophical Transactions of The Royal Society A*, Vol 255, 1963, pp. 469–503. https://doi.org/10.1098/rsta.1963.0010.

[13] Ffowcs Williams, J. E., Hawkings, D. L., "Sound generation by turbulence and surfaces in arbitrary motion," *Philosophical Transactions of The Royal Society A*, Vol. 264, 1969, 32142. https://doi.org/10.1098/rsta.1969.0031.

[14] Goldstein, M.E., "A unified approach to some recent developments in jet noise theory," *International Journal of Aeroacoustics,* Vol.1, pp. 1-16, 2002. https://doi.org/10.1260/1475472021502640.

[15] Goldstein, M.E., "A generalized acoustic analogy," Journal of Fluid Mechanics, Vol. 488, 2003, pp. 315-333. https://doi.org/10.1017/S0022112003004890.

[16] Goldstein, M.E., Leib, S. J., "The Aero-acoustics of slowly diverging supersonic jets," *Journal of Fluid Mechanics*., Vol. 600, 2008. https://doi.org/10.1017/S0022112008000311.

[17] Leib, S.J., Goldstein, M.E., "Hybrid Source Model for Predicting High-Speed Jet Noise" *AIAA Journal*, Vol. 49(7), 2011, pp.1324–1335, 2011. https://doi.org/10.2514/1.J050707.

[18] Karabasov, S.A., Afsar, M.Z., Hynes, T.P., Dowling, A.P., McMullan, W.A., Pokora, C.D., Page, G.J., McGuirk, J.J., "Jet Noise: Acoustic Analogy informed by Large Eddy Simulation," *AIAA Journal*., Vol. 48(7), 2010. https://doi.org/10.2514/1.44689.

[19] Depuru Mohan, N.K., Dowling, A.P., Karabasov, S.A., Xia, H., Graham, O. Hynes, T.P., Tucker, P.G., "Acoustic sources and far-field noise of chevron and round jets," *AIAA Journal*, Vol. 53(9), 2015. https://doi.org/10.2514/1.J052973.

[20] Karabasov, S.A. Bogey, C., Hynes, T.P., "An investigation of the mechanisms of sound generation in initially laminar, subsonic jets using the Goldstein acoustic analogy," *Journal of Fluid Mechanics*. Vol. 714, pp. 24 – 57, 2013. https://doi.org/10.1017/jfm.2012.448.

[21] Semiletov, V.A., Karabasov, S.A., "A volume integral implementation of the Goldstein generalised acoustic analogy for unsteady flow simulations," *Journal of Fluid Mechanics*, Vol. 853, 2018, pp.461-487. https://doi.org/10.1017/jfm.2018.572.

[22] SILOET Programme Rolls-Royce private data.

[23] Bridges,J., Wernet, M., "Establishing Consensus Turbulence Statistics for Hot Subsonic Jets," 16th *AIAA/CEAS Aeroacoustics Conference,* 2010. https://doi.org/10.2514/6.2010-3751

[24] Bridges, J. And Wernet, M.P., "The NASA Subsonic Jet Particle Image Velocimetry (PIV) Dataset", 2011, NASA/TM-2011-216807

[25] Gryazev, V., Karabasov, S.A., "Comparison of two Goldstein acoustic analogy implementations with the Tam&Auriault model for heated and unheated jet noise prediction", *AIAA Aeroacoustics Conference*, 25-29 June, Atlanta, 2018. https://doi.org/10.2514/6.2018-2828.

[26] Tam, C.K.W., Auriault, L., "Mean flow refraction effects on sound from localized sources in a jet," *Journal of Fluid Mechanics*, Vol. 370, pp. 149-174, 1998. https://doi.org/10.1017/S0022112098001852.

[27] Spieser, E., Bailly C., "Sound propagation using an adjoint-based method," *Journal of Fluid Mechanics*, Volume 900, 2020. https://doi.org/10.1017/jfm.2020.469.

[28] Gryazev, V., Markesteijn, A.P., Karabasov, S.A., "Low-Order Models of Dual-Stream Jet Noise with Temperature Effects Based on the Goldstein Generalised Acoustic Analogy," *25th AIAA/CEAS Aeroacoustics Conference*, 20 - 23 May 2019, Delft, The Netherlands. https://doi.org/10.2514/6.2019-2665.

[29] Karabasov, S.A., Goloviznin, V.M., "Compact Accurately Boundary Adjusting high-REsolution Technique for Fluid Dynamics," *Journal of Computational Physics*, Vol. 228, 2009, pp. 7426-7451. https://doi.org/10.1016/j.jcp.2009.06.037.

[30] Goloviznin, V.M., Samarskii. A.A., "Finite difference approximation of convective transport equation with space splitting time derivative," Journal of Mathematical Modelling, 1998, Vol. 10(1), 86–100.

[31] Faranosov, G.A., Goloviznin, V.M., Karabasov, S.A., Kondakov, V.G., Kopiev, V.F., Zaitsev, M.A., "CABARET method on unstructured hexahedral grids for jet noise computation," *Computers & Fluids*, Vol. 88, pp. 165-179, 2013.

[32] Semiletov, V.A., Karabasov, S.A., "CABARET scheme with conservation-flux asynchronous timestepping for nonlinear aeroacoustics problems," *Journal of Computational Physics*, Vol. 253, pp. 157-165, 2013. doi:10.1016/j.jcp.2013.07.008.

[33] Fureby, C., Grinstein, F.F., "Large Eddy Simulation of High Reynolds Number Free and Wall Bounded Flows," Journal of Computational Physics, Vol. 181, pp. 68-97, 2002. https://doi.org/10.1006/jcph.2002.7119.

[34] Markesteijn, A.P., Semiletov, V.A., Karabasov, S.A., "GPU CABARET solutions for the SILOET jet noise experiment: Flow and noise modelling," *22nd AIAA/CEAS Aeroacoustics Conference*, Lyon, France 2016. https://doi.org/10.2514/6.2016-2967.

[35] Markesteijn, A.P., Karabasov, S.A., "CABARET solutions on graphics processing units for NASA jets: Grid sensitivity and unsteady inflow condition effect," Comptes Rendus Mécanique, Vol. 346 (10), pp. 948-963, 2018. https://doi.org/10.1016/j.crme.2018.07.004.

[36] Markesteijn, A.P., Karabasov, S.A., "Simulations of co-axial jet flows on graphics processing units: The flow and noise analysis," *Philosophical Transactions of The Royal Society A*, Vol. 377, 2019. https://doi.org/10.1098/rsta.2019.0083.

[37] Markesteijn, A.P., Gryazev, V., Karabasov, S.A., Ayupov, R.Sh., Benderskiy, L. A., Lyubimov, D.A. "Flow and Noise Predictions of Coaxial Jets", *AIAA Journal*, Vol. 58(12), 2020. https://doi.org/10.2514/1.J058881.

[38] Shur, M. L., Spalart, P., Strelets, M., "Noise Prediction for Increasingly Complex Jets. Part I: Methods and Tests," *International Journal of Aeroacoustics*, Vol. 4(3), 2005. https://doi.org/10.1260/1475472054771376.

[39] Khavaran, A., Bridges, J., "SHJAR Jet Noise Data and Power Spectral Laws," NASA/TM—2009-215608, http://gltrs.grc.nasa.gov, March 2009.

[40] Khavaran, A., Bridges, J., "Development of Jet Noise Power Spectral Laws Using SHJAR Data," *15th AIAA/CEAS Aeroacoustics Conference,* Miami, Florida, May 2012. https://doi.org/10.2514/6.2009-3378.

[41] Markesteijn, A.P., Karabasov, S. A., "GPU-CABARET Solutions for the NASA SHJAR Jet Noise Experiment: Flow and Noise Modeling," 23rd AIAA/CEAS Aeroacoustics Conference, 2017. https://doi.org/10.2514/6.2017-3852

[42] Tam, C.K.W., Ganesan, A., "A Modified kappa - epsilon Turbulence Model for Calculating the Mean Flow and Noise of Hot Jets," *AIAA Journal*, Vol. 42, No. 1, pp. 2634, 2004. https://doi.org/10.2514/1.9027.

[43] Khavaran, A., Bridges, J., "An Empirical Temperature Variance Source Model in Heated Jets," NASA Technical Memorandum, 2012

[44] Pope, S. B., Turbulent Flows, *Cambridge University Press*, 2000. https://doi.org/10.1017/CBO9780511840531,